Research
A SCIENCE PARTNER JOURNAL

RESEARCH ARTICLE

A Cation-Driven Approach toward Deep-Ultraviolet Nonlinear Optical Materials

Cong Hu[1,2†], Meng Cheng[1,2†], Wenqi Jin[1,2], Jian Han[1,2], Zhihua Yang[1,2*], and Shilie Pan[1,2*]

[1]Research Center for Crystal Materials, CAS Key Laboratory of Functional Materials and Devices for Special Environments, Xinjiang Technical Institute of Physics & Chemistry, CAS,40–1 South Beijing Road, Urumqi 830011, China. [2]Center of Materials Science and Optoelectronics Engineering, University of Chinese Academy of Sciences, Beijing 100049, China.

*Address correspondence to: zhyang@ms.xjb.ac.cn (Z.Y.); slpan@ms.xjb.ac.cn (S.P.)
†These authors contributed equally to this work.

Citation: Hu C, Cheng M, Jin W, Han J, Yang Z, Pan S. A Cation-Driven Approach toward Deep-Ultraviolet Nonlinear Optical Materials. *Research* 2023;6:Article 0053. https://doi.org/10.34133/research.0053

Submitted 20 November 2022
Accepted 2 January 2023
Published 9 March 2023

Copyright © 2023 Cong Hu et al. Exclusive Licensee Science and Technology Review Publishing House. No claim to original U.S. Government Works. Distributed under a Creative Commons Attribution License (CC BY 4.0).

The design of new materials with special performances is still a great challenge, especially for the deep-ultraviolet nonlinear optical materials in which it is difficult to balance large bandgaps and strong second harmonic generation responses due to their inverse relationship. Cation variation not only influences the whole structure frameworks but also directly participates in the formation of electronic structures, both of which could lead to the uncontrollability of the properties of the designed materials. Here, a novel approach, aiming at purposeful and foreseeable material designs, is proposed to characterize the role of cations. By the verification of several series of borates, the influences of cation variation on property changes are explored systematically. Accordingly, a feasible strategy of designing deep-ultraviolet nonlinear optical materials by substituting barium for lead has been concluded, which could obviously blue-shift the ultraviolet cutoff edge and maintain the relatively strong second harmonic generation response (more than 2 times of KH_2PO_4), achieving the property optimization, and especially works efficiently in fluorooxoborates. The property optimization design strategy and the cation characterization method are not only helpful in exploring nonlinear optical materials but also enlightening in material design and selection.

Introduction

Aiming at desirable performances, the material exploration assisted by quantum chemical calculation on computers has led to many new approaches, such as high-throughput screening and machine learning in data mining, or structure prediction by exploratory algorithms [1,2]. With the great demand in laser photolithography, micro-nano processing, optical communication, and medical treatment [3–10], a series of nonlinear optical (NLO) crystals have been discovered and commercialized successfully [11–17]. At present, deep-ultraviolet (DUV) NLO materials particularly attract many academic and commercial interests as the frequency conversion core to achieve coherent light with large photon flow and ultrahigh resolution and are expected to break the "200 nm wall"[18]. However, a large bandgap ($E_g > 6.2$ eV) is indispensable for DUV transparency, while E_g is inversely proportional to the second harmonic generation (SHG) response (d_{ij}) [19]. Therefore, how to satisfy the balance between the two critical performances (E_g and d_{ij}) is a key factor in the design of outstanding DUV NLO materials. $KBe_2BO_3F_2$ (KBBF) exhibits excellent properties as a promising DUV NLO crystal [20,21], but the toxicity and layer-growing habit seriously impede its application. Finding KBBF replacements and balancing E_g and d_{ij} in the DUV region are still urgent.

To guarantee appropriate E_g and d_{ij} of designed NLO materials, several advantageous NLO-active (the sources of NLO effects) anion units are introduced, such as conjugated π configurations $[BO_3]^{3-}$, $[B_3O_6]^{3-}$, distorted d^0 or d^{10} transition-metal-centered (V^{5+}, Cd^{2+}) polyhedra, fluorooxoborate anionic units $[BO_nF_{4-n}]^{(n+1)-}$ ($n = 1$, 2, 3), and so on [22–25]. Actually, as parts of the whole electron structures, A-site metal cations could also directly influence the optical properties besides the size effects in crystal structures, but a special study of the role of cation variation is rare. Here, a convenient cation characterization approach, "Cation differentiation by electron spatial distribution" (CRESD), is proposed to distinguish the role of cations in optical properties, and an accompanying design strategy is concluded from cation variation to achieve property optimization, for example, balancing large E_g and large d_{ij} in the DUV region. We note that the property optimization strategy and cation characterization approach can be applied in the design of high-performance materials not only for the NLO functions but also for other objects, such as perovskite solar cells.

Results and Discussion

Design strategy based on cations

Along with the increase of E_g, the SHG response of typical NLO materials [26–50] demonstrates an obvious downward trend as shown in Fig. 1 (more details are shown in Table S1 in the Supplementary Materials). It is noteworthy that the compounds with outstanding SHG response (compared to $d_{36} = 0.39$ pm/V

of KH_2PO_4 [KDP]) in different bandgap regions (or ultraviolet [UV] cutoff ranges) are highlighted in Fig. 1, especially, (I) 3 to 4 eV, Bi_3TeBO_9 (20.0 KDP) [51]; (II) 4 to 5 eV, $CsPbCO_3F$ (13.4 KDP) [52] and BiB_2O_4F (12.0 KDP) [53]; (III) 5 to 6 eV, $PbB_2O_3F_2$ (13.0 KDP) [54]; (IV) 6 to 7 eV, β-BaB_2O_4 (BBO, 5.7 KDP) [55] and $K_3B_6O_{10}Cl$ (KBOC, 4.0 KDP) [56]; and (V) > 7 eV, CsB_3O_5 (CBO, 2.7 KDP) [57], LiB_3O_5 (LBO, 2.7 KDP) [58], $NH_4B_4O_6F$ (ABF, 3.0 KDP) [59], and KBBF (1.2 KDP) [21]. Among the above materials, four compounds exhibit a remarkably large SHG response, more than 10 times that of KDP, and half of the four ones contain lead atoms. However, commercialized applications of lead-containing NLO materials would face two shortcomings, narrow bandgaps, which is one of the main obstacles to the practical DUV applications, and the nonnegligible toxicity of lead cations. The unbalanced performances drive the combination properties of lead borates to be optimized.

To verify the feasibility of property optimization by the design strategy of cations, six lead borates with hierarchical SHG responses, from 3.5 to 13.4 KDP, are selected: $Pb_2Ba_3(BO_3)_3Cl$ [31], $Pb_3B_6O_{11}F_2$ [35], $Pb_2B_5O_9Cl$ [60], Pb_2BO_3Br [28], $PbB_5O_7F_3$ [61], and $PbB_2O_3F_2$ [54], which crystallize in the noncentrosymmetric space groups, $C222_1$ (No. 20), $P2_1$ (No. 4), $Pnn2$ (No. 34), $P321$ (No. 150), $Cmc2_1$ (No. 36), and $P31m$ (No. 157), respectively. The isostructural barium borates of the first 3 have been reported previously, namely, $Ba_5(BO_3)_3Cl$ [62], $Ba_3B_6O_{11}F_2$ [40], and $Ba_2B_5O_9Cl$ [63]. It notes that between $Pb_2Ba_3(BO_3)_3Cl$ and $Ba_5(BO_3)_3Cl$, the substitution from Pb^{2+} to Ba^{2+} only exists in the 8*c* cation Wyckoff positions, while Ba^{2+} in two 4*b* and one 4*a* positions are retained. In $Pb_2Ba_3(BO_3)_3Cl/Ba_5(BO_3)_3Cl$, the anionic framework is formed by noncondensed BO_3 units, while both $Pb_2B_5O_9Cl/Ba_2B_5O_9Cl$ and $Pb_3B_6O_{11}F_2/Ba_3B_6O_{11}F_2$ possess a 3-dimensional B-O network consisting of BO_3 and BO_4 units (Fig. 2A to C). Theoretical structural models Ba_2BO_3Br, $BaB_5O_7F_3$, and $BaB_2O_3F_2$ ($BaB_2O_3F_2$-$P31m$, hereinafter referred to as $BaB_2O_3F_2$) are derived from Pb_2BO_3Br, $PbB_5O_7F_3$, and $PbB_2O_3F_2$ by cation substitutions, in which the anion frameworks are formed by a noncondensed BO_3 group, a $[B_5O_7F_3]_\infty$ layer, and a $[B_6O_9F_6]_\infty$ layer, respectively. It should be noticed that the connection of the halide atoms is also different, where F in the fluorooxoborate unit BO_3F connects both with the metal Ba and B atoms, while Br connects only to the metal Ba (Fig. 2D to F). The structural information of predicted Ba_2BO_3Br, $BaB_5O_7F_3$, and $BaB_2O_3F_2$ are shown in Tables S2–S4, and their crystallographic details (atomic coordinates, bond distances, angles, etc.) have been listed in Tables S5–S12.

In addition, recently, a noncentrosymmetric $BaB_2O_3F_2$ with lower symmetry, $P2_1$, was successfully synthesized by our group [64]. The relative total energy (Helmholtz free energy) calculated by DFT (density functional theory) between predicted $BaB_2O_3F_2$ ($P31m$) and experimental $BaB_2O_3F_2$ ($P2_1$) is less than 20 meV/atom (Fig. 3), and the formation enthalpy of $BaB_2O_3F_2$ ($P31m$) is 0.024 eV/atom, and there is no imaginary phonon mode in the phonon spectrum of $BaB_2O_3F_2$ ($P31m$) (Fig. S1), indicating the thermodynamical metastability and kinetical stability. Moreover, for comparison, the structure of $PbB_2O_3F_2$ ($P2_1$) is built by a cation substitution for experimental $BaB_2O_3F_2$ ($P2_1$), and the relative total energy between $PbB_2O_3F_2$ ($P2_1$) and experimental $PbB_2O_3F_2$ ($P31m$) is about 20 meV/atom, and the formation enthalpy of $PbB_2O_3F_2$ ($P2_1$) is −0.023 eV/atom, which

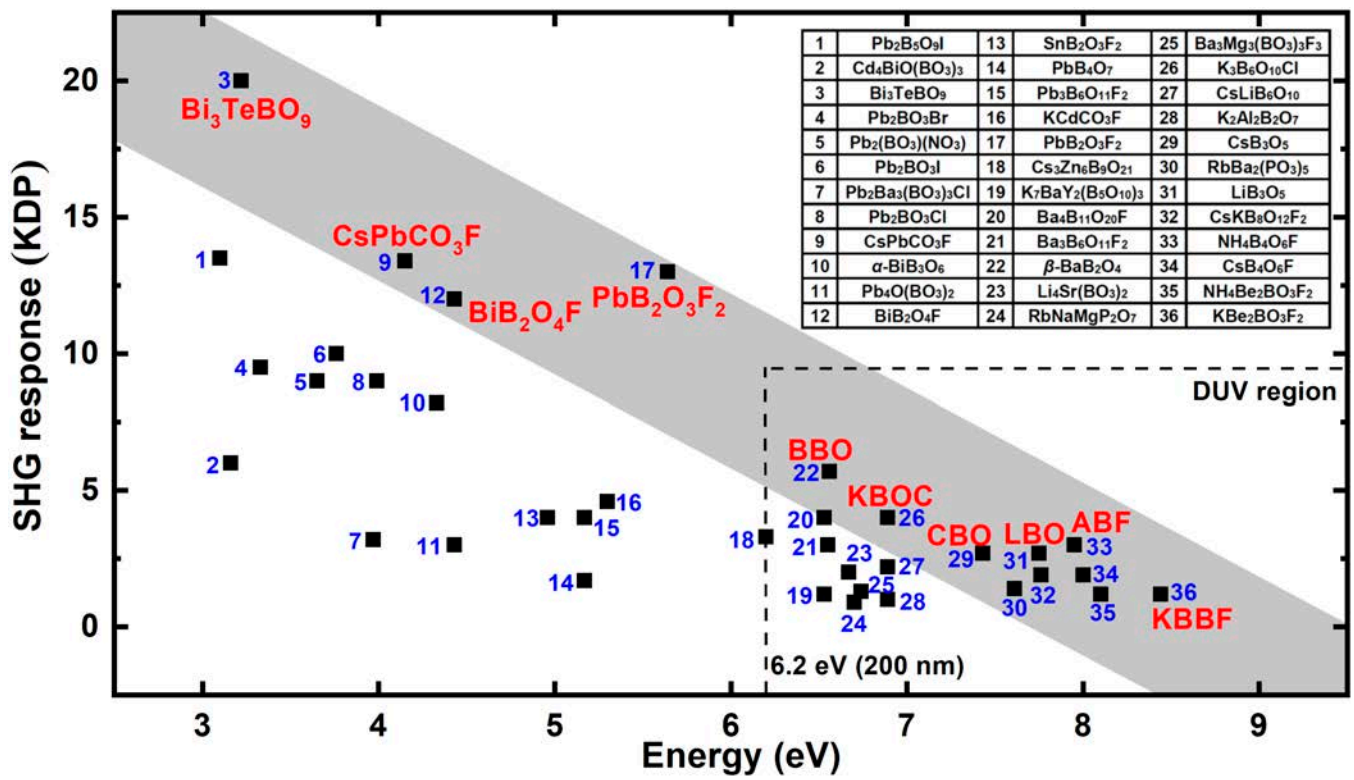


Fig. 1. Comparison of typical NLO materials on bandgap and SHG response. Nonlinear optical (NLO); second harmonic generation (SHG). Several famous NLO crystals and promising materials with outstanding SHG responses are highlighted in the different bandgap regions: (I) 3 to 4 eV, Bi_3TeBO_9 (20.0 KDP); (II) 4 to 5 eV, $CsPbCO_3F$ (13.4 KDP) and BiB_2O_4F (12.0 KDP); (III) 5 to 6 eV, $PbB_2O_3F_2$ (13.0 KDP); (IV) 6 to 7 eV, BBO (5.7 KDP) and $K_3B_6O_{10}Cl$ (4.0 KDP); (V) >7 eV, CBO (2.7 KDP), LBO (2.7 KDP), ABF (3.0 KDP), and KBBF (1.2 KDP).

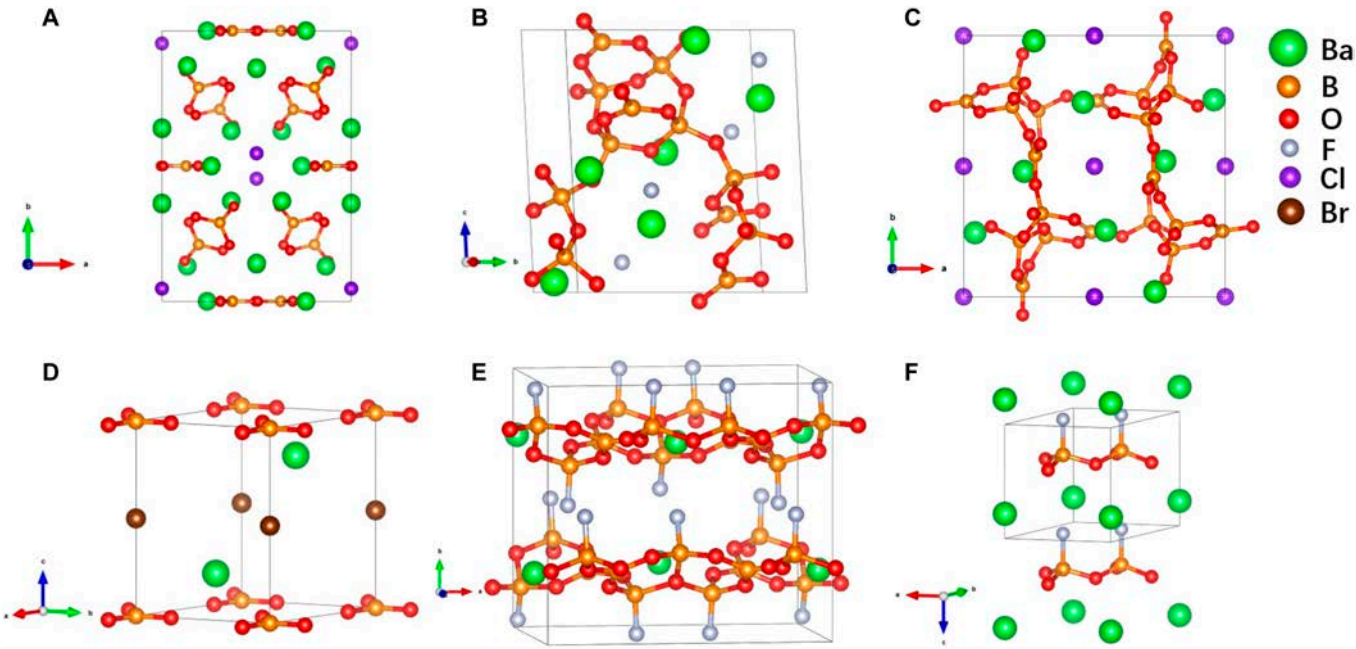


Fig. 2. Crystal structures of barium borates after cation substitutions, $Ba_5(BO_3)_3Cl$ (A), $Ba_3B_6O_{11}F_2$ (B), $Ba_2B_5O_9Cl$ (C), Ba_2BO_3Br (D), $BaB_5O_7F_3$ (E), and $BaB_2O_3F_2$ (*P*31*m*) (F).

shows the thermodynamical possibility of being synthesized. Here, the formation enthalpies of $BaB_2O_3F_2$ (*P*31*m*) and $PbB_2O_3F_2$ ($P2_1$) are calculated from the general experimental source, B_2O_3, and BaF_2/PbF_2.

CRESD method

To clarify the role of cations in property changes, the CRESD method is proposed to characterize the volumetric effects of various metal cations by the occupied volume of electrons, namely, electron spatial distribution (ESD). Taking the above isostructural substitutions of lead/barium borates as examples, the magnitudes of ESD between lead and barium atoms are compared on the basis of atom radius R(M), cation radius $R(M^{2+})$, and cation volume $V(M^{2+})$, where $V(M^{2+}) = (2 \times R(M^{2+}))^3$ (Table 1). Here, deviation γ is defined as $(P_1 - P_2)/((P_1+P_2)/2)$ to evaluate the differentiation of P_1 and P_2, where parameter *P* could be the magnitudes of ESD based on atom/cation radius and cation volume, or any other parameters, such as crystal volume, in the following contents. The deviations γ of Pb^{2+}/Ba^{2+} ESD based on R(M), $R(M^{2+})$, and $V(M^{2+})$ are 21.4%, 13.3%, and 39.5%, respectively. Considering the isostructural substitutions, the deviation γ of ESD between Pb^{2+} and Ba^{2+} should change slightly. ESD $[R(M^{2+})]$ is better to characterize the cations but hard to sum arithmetically for composite cations. ESD $[V(M^{2+})]$ can also be summed arithmetically, but its deviation γ is too large. More importantly, all of the above ESD values are incapable of ion groups, such as $[NH_4]^+$, $[CH_3NH_3]^+$, and so on. Consequently, ESD based on Bader volumes could overcome the above restrictions, where the electron density in the whole space is partitioned by DFT calculation [65,66], and hereinafter the ESD refers to the results on Bader volumes. Pb^{2+} and Ba^{2+} have similar values of ESD, and their deviations γ are 6.7%, 8.7%, and 9.0% in $M_2Ba_3(BO_3)_3Cl$, $M_3B_6O_{11}F_2$, and $M_2B_5O_9Cl$ ($M = Pb^{2+}$, Ba^{2+}), all of which are lower than that of ESD $[R(M^{2+})]$ (Table 2), indicating that the ESD changes slightly in isostructural substitution.

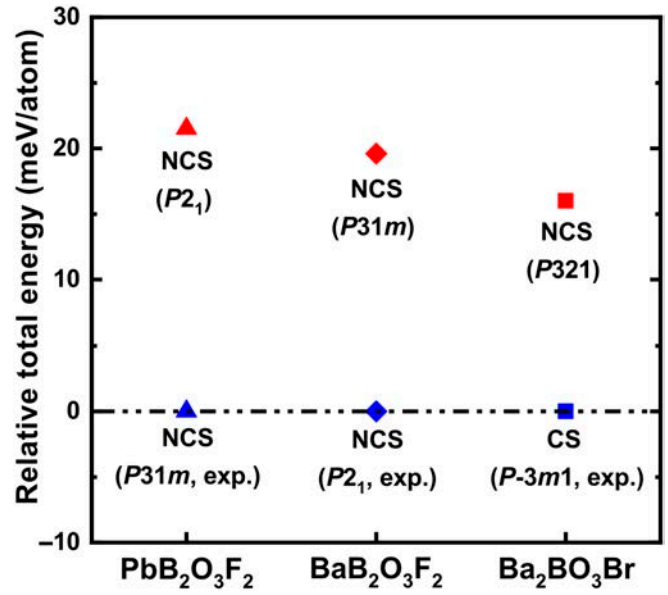


Fig. 3. Relative total energy between theoretical (red) and experimental (blue) structures in $PbB_2O_3F_2$, $BaB_2O_3F_2$, and Ba_2BO_3Br.

ESD can be not only applied in the comparison of experimental structures but also introduced to analyze the change regulations on structures and performances of theoretical structures, such as Ba_2BO_3Br and $BaB_2O_3F_2$ mentioned above. As the lattice parameters are relaxed in geometric structure optimization, the values of ESD have been calculated from both optimized and experimental (no-optimization) structures. The ESD and crystal volume in Pb_2BO_3Br are 27.7/28.3 and 143.6/149.0 $Å^3$ without/with optimization, and their deviation γ is 2.2% and 3.7% (Table S2), indicating the feasibility of structure optimization. Interestingly, the ESD of Pb/Ba in

Table 1. Comparison between lead and barium elements of ESD based on atom radius R(M), valence state radius R(M^{2+}), and ionic volume V(M^{2+}).

	ESD[R(M)] (Å)	ESD[R(M^{2+})] (Å)	ESD[V(M^{2+})] [b] ($Å^3$)
Pb	1.75	1.19	13.5
Ba	2.17	1.36	20.1
Deviation γ [a]	21.4%	13.3%	39.5%

[a]Deviation γ, for example, is defined as $\gamma = \frac{P(Ba) - P(Pb)}{(P(Ba) + P(Pb))/2}$, where *P* is the magnitude of ESD based on radius R or volume V. Electron spatial distribution (ESD).
[b]ESD based on ionic volume is calculated by ESD[V(M^{2+})] = $(2 \times R(M^{2+}))^3$

Table 2. Comparison between lead and barium compounds of cation ESD based on Bader volumes.

Compound A	ESD ($Å^3$)	Compound B	ESD ($Å^3$)	Deviation γ
$Pb_2Ba_3(BO_3)_3Cl$	23.1 (Pb1)	$Ba_5(BO_3)_3Cl$	24.7 (Ba1)	6.7%
$Pb_3B_6O_{11}F_2$	22.6 (Pb1)	$Ba_3B_6O_{11}F_2$	24.2 (Ba1)	6.8%
	22.0 (Pb2)		24.0 (Ba2)	8.7%
	21.3 (Pb3)		23.7 (Ba3)	10.7%
			Average	8.7%
$Pb_2B_5O_9Cl$	22.7 (Pb1)	$Ba_2B_5O_9Cl$	24.2 (Ba1)	6.4%
	22.0 (Pb2)		24.7 (Ba2)	11.6%
			Average	9.0%
Pb_2BO_3Br	28.3 (Pb1)	Ba_2BO_3Br	32.5 (Ba1)	13.9%
$PbB_5O_7F_3$	21.5 (Pb1)	$BaB_5O_7F_3$	24.2 (Ba1)	11.8%
$PbB_2O_3F_2$	22.0 (Pb1)	$BaB_2O_3F_2$	23.3 (Ba1)	5.7%

Pb_2BO_3Br/Ba_2BO_3Br is 28.3/32.5 $Å^3$, distinctly larger than those of the other 4 couples of lead/barium borates, ~22.0/24.0 $Å^3$, and the deviation γ of cation ESD is 13.9%, the largest one among the 6 couples of lead/barium borates. The reason mainly comes from incompact structures. Pb_2BO_3Br/Ba_2BO_3Br belongs to rich metal borates with metal:boron = 2:1, resulting in the delocalization of electrons around metals, where the evidence is the larger deviation γ of crystal volumes between Pb_2BO_3Br and Ba_2BO_3Br, 18.6%. On the contrary, $PbB_2O_3F_2/BaB_2O_3F_2$ contains fewer metal atoms, metal:boron = 1:2, and the cation ESD is also relatively small, 22.0/22.3 $Å^3$. The deviation γ of ESD is the smallest, 5.7%, and the deviation γ of crystal volumes is only 3.0% (Table S3).

Property optimization for balancing bandgaps and SHG responses

To assess the influence of cation variation on property change, the optical properties of the selected lead/barium borates are evaluated and analyzed in detail by DFT calculation. Based on generalized gradient approximation (GGA)-Perdew-Burke-Ernzerhof (PBE) functionals, the calculated bandgaps of these lead borates, $Pb_2Ba_3(BO_3)_3Cl$, $Pb_3B_6O_{11}F_2$, and $Pb_2B_5O_9Cl$, are 3.54, 3.81, and 3.36 eV, which are lower than their experimental or HSE06 values, 3.97 eV (312 nm), 5.17 eV (240 nm), and 4.41 eV (281 nm, HSE06), respectively. Here, the underestimation of bandgaps under GGA-PBE functional is derived from the inherent discontinuous exchange-correlation energy [67], and a scissors operator is adopted as the difference between the GGA bandgap and the experimental bandgap to eliminate this underestimation in the calculation of optical properties. In addition, a more expensive calculation, hybrid functional HSE06 [68], is used to achieve the value of bandgap more accurately for the lack of experimental bandgaps.

To verify the theoretic simulations, a couple of borates, $M_2B_5O_9Cl$ (M = Pb, Ba), were synthesized in experiments, and the UV cutoff edge and SHG intensity were also measured

(powder X-ray diffraction [XRD] patterns are shown in Fig. S2). As shown in Fig. 4, the UV absorbing cutoff of $Pb_2B_5O_9Cl$ is 281 nm, which is consistent with our HSE06 calculation value of 281 nm. $Ba_2B_5O_9Cl$ shows a UV cutoff edge of 189 nm, which is similar to 185 nm in the previous work [63].

By cation substitution in the three lead borate prototypes with moderate SHG responses, the bandgaps of barium borates have increased to 5.26 eV (236 nm, HSE06), 6.53 eV (190 nm, exp.), and 6.56 eV (189 nm, exp., this work) for $Ba_5(BO_3)_3Cl$, $Ba_3B_6O_{11}F_2$, and $Ba_2B_5O_9Cl$, which exhibit 76, 50, and 92 nm blue-shift from the isostructural lead borates. Correspondingly, the SHG responses have changed to 0.5, 3.0, and 0.7 KDP for $Ba_5(BO_3)_3Cl$, $Ba_3B_6O_{11}F_2$, and $Ba_2B_5O_9Cl$ from 3.2, 4.0, and 1.2 KDP of $Pb_2Ba_3(BO_3)_3Cl$, $Pb_3B_6O_{11}F_2$, and $Pb_2B_5O_9Cl$. The experimental SHG intensities of $M_2B_5O_9Cl$ (M = Pb, Ba) are shown in the insets of Fig. 4. It is noted that both $Ba_3B_6O_{11}F_2$ and $Ba_2B_5O_9Cl$ have obtained DUV cutoff edges (<200 nm), but only borate fluoride $Ba_3B_6O_{11}F_2$ maintained relatively strong SHG responses (> 2 KDP). For the last three prototypes, borate halide Pb_2BO_3Br and fluorooxoborates $PbB_5O_7F_3$ and $PbB_2O_3F_2$ exhibit remarkably strong SHG responses, 9.5, 6.0, and 13.0 KDP, but their bandgaps are different, 3.33 eV (372 nm), 5.51 (225 nm), and 5.64 eV (220 nm), respectively. After cation substitutions, the combination property of the former changes slightly, 3.87 eV (320 nm) and 7.8 KDP for Ba_2BO_3Br. Contrarily, $BaB_5O_7F_3$ and $BaB_2O_3F_2$ show a great change in their prototype, 7.92 eV (157 nm) with 2.5 KDP, and 8.24 eV (150 nm) with 4.8 KDP. Furthermore, to analyze the source of the variation in bandgaps among the above metal borates, the total and partial density of states are shown in Figs. S3 to S8. Compared to the partial density of states among these metal borates, it is found that the conduction band minima are mainly composed of Pb-p or Ba-d and a little of B-p orbitals, while the valence band maxima mainly contain O-p, a little of halogen p orbitals, along with slight Pb/Sn-s orbitals for the stereochemically active lone pairs. According to the revised lone pair model [69], the interaction between Pb and O drives from the mixture of empty Pb p and a filled antibonding state between Pb-s and O-p states in PbO, and the lone pair stereochemical activity of Pb cations greatly influences the reduction of bandgaps in series of metal borates [70]. Therefore, the cation substitution from Pb to Ba could avoid the stereochemical activity of the lone pairs to achieve a relatively large bandgap, a similar effect that introducing the F atom could eliminate the dangling bonds of BO_3 groups in a series of fluorooxoborates [25,47,50,59]. As far as the purpose of property optimization, doubtless, the cation substitution in the fluorooxoborates $BaB_5O_7F_3$ and $BaB_2O_3F_2$ is more successful.

Figure 5 shows the changes for bandgap (E_g) and SHG response in the cation substitution from lead to barium. The whole region is divided into 4 sections: I, $E_g < 6.2$ eV, SHG < 2 KDP; II, $E_g \geq 6.2$ eV, SHG < 2 KDP; III, $E_g < 6.2$ eV, SHG ≥ 2 KDP; IV, $E_g \geq 6.2$ eV, SHG ≥ 2 KDP, where 6.2 eV and 2 KDP are DUV and relatively strong SHG response bounds, respectively. Here, before the cation substitution, 5 lead borates in 6 are all located at Section III, indicating strong SHG responses but not DUV cutoff edges. After the cation substitution, these 5 barium borates scatter into 3 sections, 1 (Ba_2BO_3Br) still in Section III, 1 ($Ba_5(BO_3)_3Cl$) in Section I, and 3 in Section IV ($Ba_3B_6O_{11}F_2$, $BaB_5O_7F_3$, and $BaB_2O_3F_2$). Although $Ba_2B_5O_9Cl$ shows a DUV bandgap, its SHG response is relatively small for the reason that the SHG intensity of its prototype is not strong. It is found that these lead borates could keep strong SHG responses (≥2 KDP) after cation substitution except $Pb_2Ba_3(BO_3)_3Cl$ and $Pb_2B_5O_9Cl$, whose SHG response is the smallest among the 6 lead borates. What is more important, the bandgaps of all the lead borates have visibly widened, and especially four of them have exceeded the DUV limit (6.2 eV, 200 nm) after cation substitution. Therefore, the cation substitution from lead to barium could optimize the combination properties.

Considering the importance of SHG response for NLO materials, exploring the role of cation variation on SHG response is vital to deepen the understanding of the structure–property relationship. The real-space atom-cutting technique is an efficient postprocessing tool to evaluate the contribution of microscopic structural groups to optical properties, such as the SHG coefficient. Table 3 shows the results of the calculated SHG coefficients before (original) and after (e.g., cut Pb) cutting the metal cations, and the "SHG reducing" is expressed as "SHG

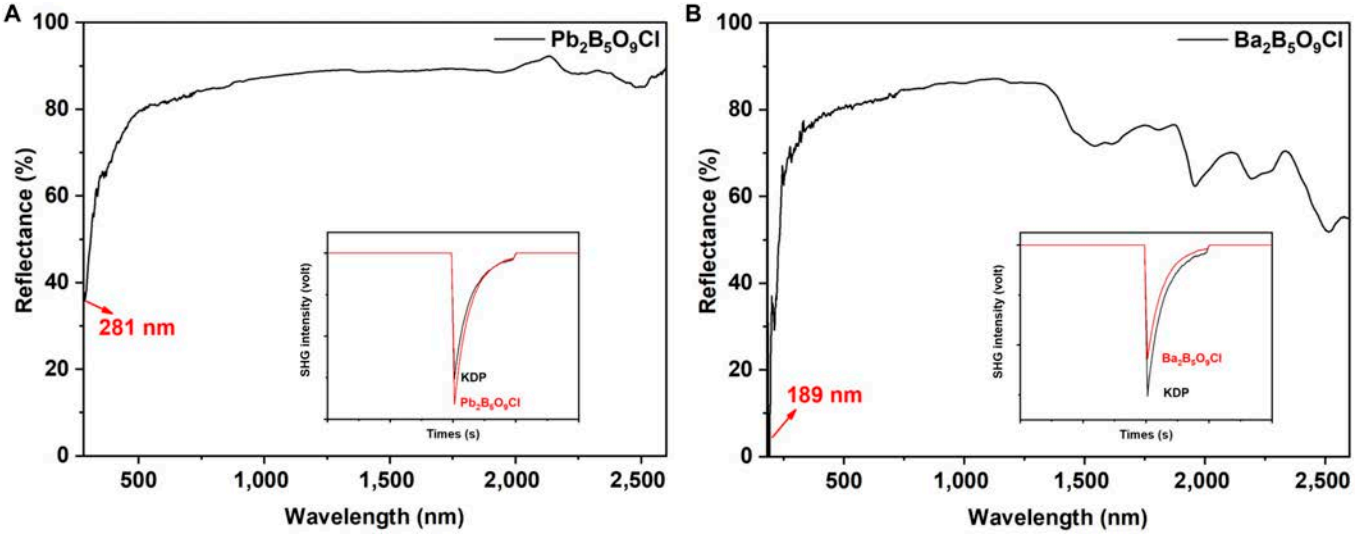


Fig. 4. Ultraviolet–visible–near infrared diffuse reflectance spectrum of $Pb_2B_5O_9Cl$ (A) and $Ba_2B_5O_9Cl$ (B). The insets are SHG intensity oscilloscope traces.

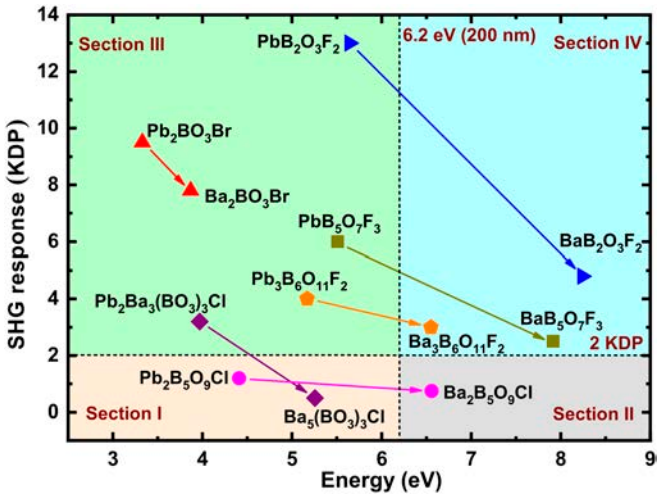


Fig. 5. Property changes from lead borates to barium borates. Changes in optical properties (SHG response and bandgap), and the classifications of four value sections based on the DUV (200 nm) and relatively strong SHG response (2 KDP) bounds in the cation substitution from lead to barium. Deep-ultraviolet (DUV); second harmonic generation (SHG).

(reducing) = 1 − SHG (cut)/SHG (original)", which is related to the contribution of metal cations to SHG coefficients. Various nonzero components of SHG coefficients are related to the different symmetries of the point groups (relatively small values, < 0.1 pm/V, are not listed here), and the final SHG response is characterized by the largest SHG coefficient in the effective SHG formula. The results indicate that in $Ba_3B_6O_{11}F_2$ and $Ba_2B_5O_9Cl$, lead and barium cations contribute equally to the SHG coefficient. In $M(BO_3)_3Cl$ (M = Pb_2Ba_3, Ba_5), the Wyckoff site cations cause various contributions to the SHG coefficient d_{14}. Namely, in $Pb_2Ba_3(BO_3)_3Cl$, two 8c Pb contribute the most of d_{14}, 29% in 33%, and two 4b Ba and one 4a Ba contribute the relatively small parts, 7% and 0.3% in 33%, respectively. In $Ba_5(BO_3)_3Cl$, two 8c Ba contribute almost all of the d_{14}, but 4a Ba makes a remarkably negative contribution, −30%, which leads to an obvious decrease of the SHG response from $Pb_2Ba_3(BO_3)_3Cl$ to $Ba_5(BO_3)_3Cl$. For $MB_5O_7F_3$ (M = Pb, Ba), the metal cations contribute about 10% to 15%, and the relatively small contribution mainly derives from the ratio of metal cations to B-O/B-O-F anion groups is only 1:5.

Furthermore, in $M_2BO_3Br_2$ and $MB_2O_3F_2$ (M = Pb, Ba), the cations exert a remarkable contribution to the SHG responses. In addition, in the SHG density map (Fig. S9), there are plenty of unoccupied states contributing to the VE and virtual-hole (VH) process and occupied states contributing to the VH process around Pb and Ba. In $MB_2O_3F_2$ (M = Pb, Sn, Ba), Sn shows a vitally negative contribution for d_{33} (−130%), which is the reason that the SHG response of $SnB_2O_3F_2$ is much lower than that of isostructural $PbB_2O_3F_2$, in accordance with the results from another group [54], while Sn and Pb play similar contributions to d_{22}, 73% to 72%.

On the other hand, to explore the trends of property changing from $PbB_2O_3F_2$ to $BaB_2O_3F_2$, two virtual middle structures, $Pb_{0.75}Ba_{0.25}B_2O_3F_2$ ($Pb_{0.75}Ba_{0.25}$) and $Pb_{0.25}Ba_{0.75}B_2O_3F_2$ ($Pb_{0.25}Ba_{0.75}$) are introduced. As shown in Fig. 6A, along with the bandgap increasing, the $|d_{33}|$ and $|d_{22}|$ decrease, as the negative relationship between bandgap and SHG response. Here, we add a trend line with the formula $d = a / E_g^5$, where d and E_g are SHG coefficient and HSE06 bandgap values, and the constant a is calculated by the value of d and E_g. Of course, this formula only considers the bandgap effect and ignore the momentum matrix elements [71], so it is a very rough approximation to estimate the trends of SHG coefficients along with bandgaps semiquantitatively. Furthermore, as shown in Table S13, a single Pb atom makes much more contributions to d_{22} than Ba (22% to 4% in $Pb_{0.75}Ba_{0.25}$ and 33% to 7% in $Pb_{0.25}Ba_{0.75}$), while Pb and Ba show similar contributions to d_{33} (12% to 9% in $Pb_{0.75}Ba_{0.25}$ and 13% to 13% in $Pb_{0.25}Ba_{0.75}$). Interestingly, the contributions of a single Ba atom develop both in d_{22} and d_{33} as the proportion of Ba content increases. Therefore, the SHG coefficient trends of $PbB_2O_3F_2$, $Pb_{0.75}Ba_{0.25}$, and $Pb_{0.25}Ba_{0.75}$ do not vary so much, while the SHG coefficients of $BaB_2O_3F_2$ are much larger than the expected value according to the trend lines.

From Fig. S10, the location of Pb-6p in conduction band minimum is nearer to the Fermi surface than that of Ba-5d for the stereochemical activity of the lone pairs. Meanwhile, the $SnB_2O_3F_2$ obtains a smaller bandgap than $PbB_2O_3F_2$ for stronger stereochemical activity. Table 3 also shows that Ba^{2+} contributes the main part of d_{33} in $BaB_2O_3F_2$, so the $BaB_2O_3F_2$ could maintain a large SHG coefficient when obtaining a large bandgap. Furthermore, we also calculate the ESD value of $Pb_{0.75}Ba_{0.25}$ and $Pb_{0.25}Ba_{0.75}$ and compared them with $PbB_2O_3F_2$ and $BaB_2O_3F_2$. Then, Fig. 6B shows SHG response decreasing along with the increase of ESD in $MB_2O_3F_2$ (M = Pb, Ba). It is important to note that the above conclusion has only been obtained in the case of cation substitution between Pb and Ba in $MB_2O_3F_2$ structures.

Conclusion

Through the investigation of a series of barium borates, $Ba_5(BO_3)_3Cl$, $Ba_3B_6O_{11}F_2$, $Ba_2B_5O_9Cl$, Ba_2BO_3Br, $BaB_5O_7F_3$, and $BaB_2O_3F_2$, along with their prototypes of cation substitutions lead borates, we found that ESD is very useful to describe the electron occupied space, and the magnitudes of ESD are similar in the isostructural substitutions. As the aim of chemical substitutions is to develop performances, three cases, one borate fluoride, and two fluorooxoborates, in 6 cation substitutions from lead to barium have achieved the property optimization, enlarging bandgaps to enter the DUV region (6.2 eV, 200 nm) from outside DUV as the absence of lone pair in metal cations, and maintaining relatively strong SHG responses (> 2 KDP) for the reason that metal cations show less contribution to SHG responses than the anion frames. The cation substitution between Pb and Ba in $MB_2O_3F_2$ structures shows the negative relation between ESDs and SHG responses, which indicates the direction of searching for the NLO material with larger SHG responses. In conclusion, by analyzing the cation variations, a cation substitution approach toward DUV NLO materials has been proposed, and two predicted fluorooxoborates $BaB_5O_7F_3$ and $BaB_2O_3F_2$ have achieved the balance between large bandgaps and strong responses.

Experimental and Computational Methods

Experiment details

Solid-state synthesis

Polycrystalline samples of $Ba_2B_5O_9Cl$ and $Pb_2B_5O_9Cl$ were prepared by using standard high-temperature solid-state techniques. For $Pb_2B_5O_9Cl$, a stoichiometric mixture of $PbCl_2$ and

Table 3. Real-space atom-cutting results of SHG coefficients.

Compound		SHG Coefficient (pm/V)	SHG Reducing [a]	Compound		SHG Coefficient (pm/V)	SHG Reducing
$Pb_2Ba_3(BO_3)_3Cl$	Original	2.102 (d_{14})		$Ba_5(BO_3)_3Cl$	Original	−0.481 (d_{14})	
	Cut PbBa	1.410 (d_{14})	33%		Cut Ba	−0.426 (d_{14})	11%
	Cut Pb (8c)	1.501 (d_{14})	29%		Cut Ba (8c)	−0.273 (d_{14})	43%
	Cut Ba (4b)	1.965 (d_{14})	7%		Cut Ba (4b)	−0.485 (d_{14})	−0.8%
	Cut Ba (4a)	2.095 (d_{14})	0.3%		Cut Ba (4a)	−0.627 (d_{14})	−30%
$Pb_3B_6O_{11}F_2$	Original	0.688 (d_{14}) 2.057 (d_{16}) −0.903 (d_{22})		$Ba_3B_6O_{11}F_2$	Original	−0.469 (d_{14}) −1.104 (d_{16}) 1.109 (d_{22})	
	Cut Pb	0.588 (d_{14}) 1.150 (d_{16}) −0.835 (d_{22})	14% 44% 8%		Cut Ba	−0.416 (d_{14}) −0.680 (d_{16}) 0.995 (d_{22})	11% 38% 10%
$Pb_2B_5O_9Cl$	Original	−2.525 (d_{15}) −0.811 (d_{24}) 1.094 (d_{33})		$Ba_2B_5O_9Cl$	Original	−0.742 (d_{15}) −0.473 (d_{24}) 0.766 (d_{33})	
	Cut Pb	−1.067 (d_{15}) −0.688 (d_{24}) 0.783 (d_{33})	58% 15% 28%		Cut Ba	−0.356 (d_{15}) −0.409 (d_{24}) 0.515 (d_{33})	52% 13% 33%
Pb_2BO_3Br	Original	6.182 (d_{11})		Ba_2BO_3Br	Original	3.039 (d_{11})	
	Cut Pb	1.708 (d_{11})	72%		Cut Ba	0.759 (d_{11})	75%
$PbB_5O_7F_3$	Original	2.640 (d_{15}) −1.341 (d_{24}) −1.534 (d_{33})		$BaB_5O_7F_3$	Original	1.010 (d_{15}) −0.430 (d_{24}) −0.747 (d_{33})	
	Cut Pb	2.273 (d_{15}) −1.146 (d_{24}) −1.288 (d_{33})	14% 15% 16%		Cut Ba	0.918 (d_{15}) −0.375 (d_{24}) −0.674 (d_{33})	9% 13% 10%
$PbB_2O_3F_2$	Original	−2.800 (d_{22}) −4.952 (d_{33})		$BaB_2O_3F_2$	Original	−0.809 (d_{22}) −1.881 (d_{33})	
	Cut Pb	−0.780 (d_{22}) −2.776 (d_{33})	72% 44%		Cut Ba	−0.530 (d_{22}) −0.732 (d_{33})	34% 61%
$SnB_2O_3F_2$	Original	0.938 (d_{22}) −0.849 (d_{33})					
	Cut Sn	0.254 (d_{22}) −1.956 (d_{33})	73% −130%				

[a]SHG reducing is calculated by formula: SHG(reducing) = 1 − SHG(cut)/SHG(original)

H_3BO_3 was heated at 473 K for 10 h, cooled and ground, and then heated again at 873 K for 48 h. For $Ba_2B_5O_9Cl$, a stoichiometric mixture of $BaCl_2{\cdot}2H_2O$, $BaCO_3$, $Ba(OH)_2$, and H_3BO_3 was heated at 573 K for 10 h, cooled and ground, and then heated again at 1153 K for 48 h. The starting materials of $PbCl_2$, $BaCl_2{\cdot}2H_2O$, $BaCO_3$, and H_3BO_3 were gathered from commercial sources without any purification.

Powder X-ray diffraction

XRD patterns of $Ba_2B_5O_9Cl$ and $Pb_2B_5O_9Cl$ were obtained on an automated Bruker D2 X-ray diffractometer equipped with a diffracted beam monochromator set for Cu-Kα radiation ($\lambda = 1.5418$ Å) at room temperature in the angular range of $2\theta =$ 10° to 70° with a scan step of 0.01° and a fixed counting time of 0.1 s/step.

UV-visible-near-infrared diffuse reflectance spectrum

The diffuse reflectance spectrum was measured by a Shimadzu SolidSpec-3700DUV spectrophotometer at room temperature from 175 to 2600 nm.

Second-order NLO measurements

Powder SHG effects were measured by using the Kurtz-Perry method with a Q-switched Nd: YVO_4 solid-state laser at 1064 nm [72]. Polycrystalline samples of $Ba_2B_5O_9Cl$ and $Pb_2B_5O_9Cl$ were ground and sieved into the following particle size ranges: 38 to 55, 55 to

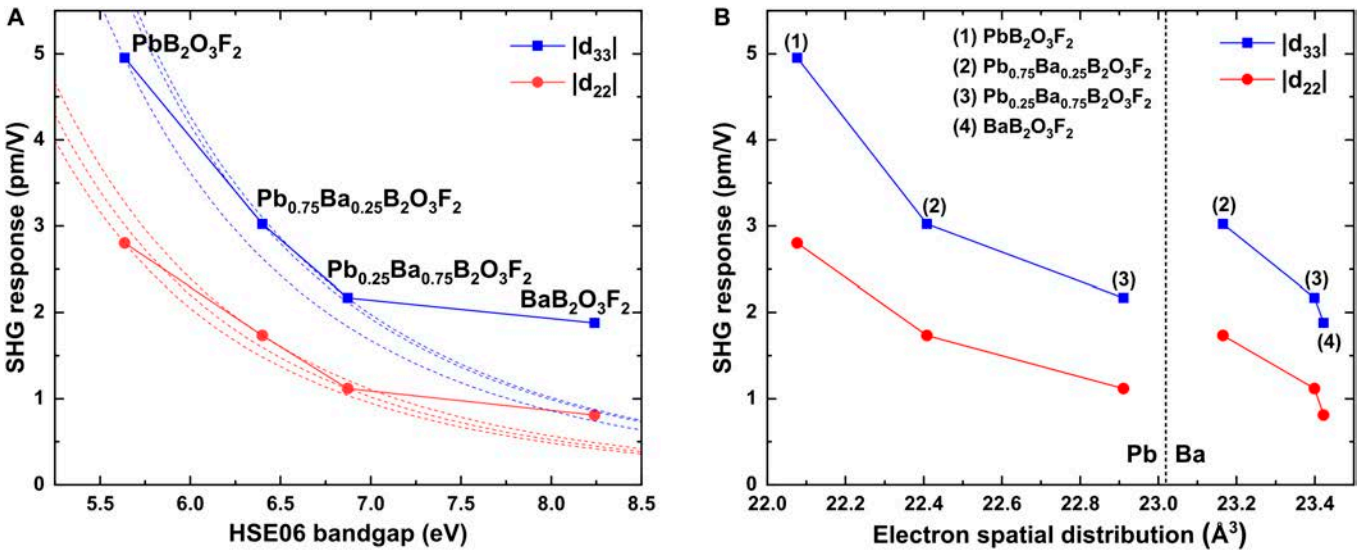


Fig. 6. SHG response decreases along with the increase of (A) bandgap and (B) electron spatial distribution (ESD) in $MB_2O_3F_2$ (M = Pb, $Pb_{0.75}Ba_{0.25}$, $Pb_{0.25}Ba_{0.75}$, Ba).

88, 88 to 105, 105 to 150, 150 to 200 μm. To make relevant comparisons with known SHG materials, the crystalline KDP sample was also ground and sieved into the same particle size ranges.

Computation details

Electronic structure calculation

In this paper, the CASTEP package, a plane wave pseudopotential method [73], was used for the DFT calculation of electronic structure properties. With the GGA-PBE functionals were chosen as the exchange-correlation functionals [74]. Norm-conserving pseudopotential [75] was used with the element valance states, Ba $5s^25p^66s^2$, Pb $5s^25p^65d^{10}6s^26p^2$, B $2s^22p^1$, O $2s^22p^4$, F $2s^22p^5$, Cl $3s^23p^5$, and Br $4s^24p^5$. The cutoff energies of $M_2Ba_3(BO_3)_3Cl$, $M_3B_6O_{11}F_2$, $M_2B_5O_9Cl$, M_2BO_3Br, $MB_5O_7F_3$ and $MB_2O_3F_2$ ($M = Ba^{2+}$, Pb^{2+}) were all no more than 940 eV and the Monkhorst-Pack k-point grids were $3 \times 3 \times 3$, $4 \times 3 \times 3$, $6 \times 1 \times 4$, $4 \times 4 \times 2$, $4 \times 4 \times 3$, and $5 \times 5 \times 4$, respectively.

SHG coefficient calculation

When the phase-matching condition is met, the SHG conversion efficiency of an NLO material is significantly determined by the SHG coefficients [76]. Also, the SHG coefficient components are relevant to second-order nonlinear susceptibilities, $d = \chi/2$. Through the result of the band structure from the CASTEP package, the second-order nonlinear susceptibilities at the limit of zero frequency, $\chi_{ijk}^{(2)}(0)$, can be expressed as the sum of the contribution of the virtual-electron processes and the VH processes [19,71].

$$\chi_{ijk}^{(2)} = \chi_{ijk}^{(2)}(VE) + \chi_{ijk}^{(2)}(VH)$$

$$\chi_{ijk}^{(2)}(VE) = \frac{e^3}{2\hbar m^3} \sum_{vcc'} \int \frac{d^3\vec{k}}{4\pi^3} P(ijk)$$
$$Im\left[p_{vc}^i p_{cc'}^j p_{c'v}^k\right]\left(\frac{1}{\omega_{cv}^3 \omega_{vc'}^2} + \frac{2}{\omega_{vc}^4 \omega_{c'v}}\right)$$

$$\chi_{ijk}^{(2)}(VH) = \frac{e^3}{2\hbar m^3} \sum_{vv'c} \int \frac{d^3\vec{k}}{4\pi^3} P(ijk)$$
$$Im\left[p_{vv'}^i p_{v'c}^j p_{cv}^k\right]\left(\frac{1}{\omega_{cv}^3 \omega_{v'c}^2} + \frac{2}{\omega_{vc}^4 \omega_{cv'}}\right)$$

Here, i, j, and k are Cartesian components, v (v') and c (c') are valence and conduction bands, and $P(ijk)$ represents full permutation.

Associated Content

Supplementary Materials

Phonon spectra, powder XRD patterns, total and partial density of states, SHG density, comparison of typical NLO materials in bandgap and SHG response, structure information of predicted structures, and real-space atom-cutting results of SHG coefficients are shown in the Supplementary Materials.

Acknowledgments

Funding: This work is supported by Key Research Program of Frontier Sciences, CAS (ZDBS-LY-SLH035), the National Natural Science Foundation of China (22193044), National Key R&D Program of China (2021YFB3601502), Natural Science Foundation of Xinjiang (2021D01E05), Xinjiang Major Science and Technology Project (2021A01001), the International Partnership Program of CAS (1A1365KYSB20200008), CAS Project for Young Scientists in Basic Research (YSBR-024). **Competing interests**: The authors declare that they have no competing financial interests. **Code availability**: In this work, the DFT calculations were performed by a licensed CASTEP package.

Data Availability

Data will be made available from the corresponding author upon reasonable request.

Supplementary Materials

Figs. S1 to S13.
Tables S1 to S14.

References

1. Oganov AR, Pickard CJ, Zhu Q, Needs RJ. Structure prediction drives materials discovery. *Nat Rev Mater*. 2019;4:331–348.
2. Kang S, Jeong W, Hong C, Hwang S, Yoon Y, Han S. Accelerated identification of equilibrium structures of multicomponent inorganic crystals using machine learning potentials. *npj Comput Mater*. 2022;8:108.
3. Becker P. Borate materials in nonlinear optics. *Adv Mater*. 1998;10(13):979–992.
4. Wright LG, Wu FO, Christodoulides DN, Wise FW. Physics of highly multimode nonlinear optical systems. *Nat Phys*. 2022;18:1018–1030.
5. Mutailipu M, Poeppelmeier KR, Pan SL. Borates: A rich source for optical materials. *Chem Rev*. 2021;121(3):1130–1202.
6. Xiong L, Wu L-M, Chen L. A general principle for DUV NLO materials: π-conjugated confinement enlarges band gap. *Angew Chem Int Ed*. 2021;60(47):25063–25067.
7. Kageyama H, Hayashi K, Maeda K, Attfield JP, Hiroi Z, Rondinelli JM, Poeppelmeier KR. Expanding frontiers in materials chemistry and physics with multiple anions. *Nat Commun*. 2018;9:772.
8. Wu C, Wu TH, Jiang XX, Wang ZJ, Sha HY, Lin L, Lin ZS, Huang ZP, Long XF, Humphrey MG, et al. Large second-harmonic response and giant birefringence of $CeF_2(SO_4)$ induced by highly polarizable polyhedra. *J Am Chem Soc*. 2021;143(11):4138–4142.
9. Li Z, Xu B, Liang D, Pan A. Polarization-dependent optical properties and optoelectronic devices of 2D materials. *Research*. 2020;2020:Article 5464258.
10. Harada JK, Charles N, Poeppelmeier KR, Rondinelli JM. Heteroanionic materials by design: Progress toward targeted properties. *Adv Mater*. 2019;31:Article 1805295.
11. Knyrim JS, Becker P, Johrendt D, Huppertz H. A new non-centrosymmetric modification of BiB_3O_6. *Angew Chem Int Ed*. 2006;45(48):8239–8241.
12. Tran TT, Young J, Rondinelli JM, Halasyamani PS. Mixed-metal carbonate fluorides as deep-ultraviolet nonlinear optical materials. *J Am Chem Soc*. 2017;139(3):1285–1295.
13. Wu B-L, Hu C-L, Mao F-F, Tang R-L, Mao J-G. Highly polarizable Hg^{2+} induced a strong second harmonic generation signal and large birefringence in $LiHgPO_4$. *J Am Chem Soc*. 2019;141(26):10188–10192.
14. Chen X, Ok KM. Recent advances in oxide-based nonlinear optical materials with wide infrared transparency beyond 6 μm. *Chem Asian J*. 2020;15(22):3709–3716.
15. Dong XH, Huang L, Hu CF, Zeng HM, Lin ZE, Wang X, Ok KM, Zou GH. $CsSbF_2SO_4$: An excellent ultraviolet nonlinear optical sulfate with a $KTiOPO_4$ (KTP)-type structure. *Angew Chem Int Ed*. 2019;58(20):6528–6534.
16. Mutailipu M, Zhang M, Zhang BB, Wang LY, Yang ZH, Zhou X, Pan SL. $SrB_5O_7F_3$ functionalized with $[B_5O_9F_3]^{6-}$ chromophores: Accelerating the rational design of deep-ultraviolet nonlinear optical materials. *Angew Chem Int Ed*. 2018;57(21):6095–6099.
17. Zhang F, Chen X, Zhang M, Jin W, Han S, Yang Z, Pan S. An excellent deep-ultraviolet birefringent material based on $[BO_2]^{\infty}$ infinite chains. *Light Sci Appl*. 2022;11:252.
18. Tran TT, Yu HW, Rondinelli JM, Poeppelmeier KR, Halasyamani PS. Deep ultraviolet nonlinear optical materials. *Chem Mater*. 2016;28(15):5238–5258.
19. Rashkeev SN, Lambrecht WRL, Segall B. Efficient ab initio method for the calculation of frequency-dependent second-order optical response in semiconductors. *Phys Rev B*. 1998;57:3905–3919.
20. Cyranoski D. China's crystal cache. *Nature*. 2009;457:953–955.
21. Chen CT, Wang GL, Wang XY, Xu ZY. Deep-UV nonlinear optical crystal $KBe_2BO_3F_2$—Discovery, growth, optical properties and applications. *Appl Phys B Lasers Opt*. 2009;97:9–25.
22. Hu C, Zhang BB, Lei B-H, Pan SL, Yang ZH. Advantageous units in antimony sulfides: Exploration and design of infrared nonlinear optical materials. *ACS Appl Mater Interfaces*. 2018;10(31):26413–26421.
23. Xia ZG, Poeppelmeier KR. Chemistry-inspired adaptable framework structures. *Acc Chem Res*. 2017;50(5):1222–1230.
24. Wu HP, Yu HW, Yang ZH, Hou XL, Su X, Pan SL, Poeppelmeier KR, Rondinelli JM. Designing a deep-ultraviolet nonlinear optical material with a large second harmonic generation response. *J Am Chem Soc*. 2013;135(11):4215–4218.
25. Zhang BB, Shi GQ, Yang ZH, Zhang FF, Pan SL. Fluorooxoborates: Beryllium-free deep-ultraviolet nonlinear optical materials without layered growth. *Angew Chem Int Ed*. 2017;56(14):3916–3919.
26. Huang Y-Z, Wu L-M, Wu X-T, Li L-H, Chen L, Zhang Y-F. $Pb_2B_5O_9I$: An iodide borate with strong second harmonic generation. *J Am Chem Soc*. 2010;132(37):12788–12789.
27. Zhang W-L, Cheng W-D, Zhang H, Geng L, Lin C-S, He Z-Z. A strong second-harmonic generation material $Cd_4BiO(BO_3)_3$ originating from 3-chromophore asymmetric structures. *J Am Chem Soc*. 2010;132(5):1508–1509.
28. Luo M, Song YX, Liang F, Ye N, Lin ZS. Pb_2BO_3Br: A novel nonlinear optical Lead borate bromine with a KBBF-type structure exhibiting strong nonlinear optical response. *Inorg Chem Front*. 2018;5(4):916–921.
29. Song J-L, Hu C-L, Xu X, Kong F, Mao J-G. A facile synthetic route to a new SHG material with two types of parallel π-conjugated planar triangular units. *Angew Chem Int Ed*. 2015;54(12):3679–3682.
30. Yu HW, Koocher NZ, Rondinelli JM, Halasyamani PS. Pb_2BO_3I: A borate iodide with the largest second-harmonic generation (SHG) response in the $KBe_2BO_3F_2$ (KBBF) family of nonlinear optical (NLO) materials. *Angew Chem Int Ed*. 2018;57(21):6100–6103.
31. Dong XY, Jing Q, Shi YJ, Yang ZH, Pan SL, Poeppelmeier KR, Young J, Rondinelli JM. $Pb_2Ba_3(BO_3)_3Cl$: A material with large SHG enhancement activated by Pb-chelated BO_3 groups. *J Am Chem Soc*. 2015;137(29):9417–9422.
32. Zou GH, Lin CS, Jo H, Nam G, You T-S, Ok KM. Pb_2BO_3Cl: A tailor-made polar Lead borate chloride with very strong second harmonic generation. *Angew Chem Int Ed*. 2016;55(39):12078–12082.
33. Hellwig H, Liebertz J, Bohatý L. Exceptional large nonlinear optical coefficients in the monoclinic bismuth borate BiB_3O_6 (*BIBO*). *Solid State Commun*. 1998;109(4):249–251.
34. Yu HW, Pan SL, Wu HP, Zhao WW, Zhang FF, Li HY, Yang ZH. A new congruent-melting Oxyborate, $Pb_4O(BO_3)_2$ with

optimally aligned BO_3 triangles adopting layered-type arrangement. *J Mater Chem*. 2012;22(5):2105–2110.
35. Li HY, Wu HP, Su X, Yu HW, Pan SL, Yang ZH, Lu Y, Han J, Poeppelmeier KR. $Pb_3B_6O_{11}F_2$: The first non-centrosymmetric lead borate fluoride with a large second harmonic generation response. *J Mater Chem C*. 2014;2(9):1704–1710.
36. Lin Y, Hu C-L, Mao J-G. $K_2Pb_3(CO_3)_3F_2$ and $KCdCO_3F$: Novel fluoride carbonates with layered and 3D framework structures. *Inorg Chem*. 2015;54(21):10407–10414.
37. Yu HW, Wu HP, Pan SL, Yang ZH, Hou XL, Su X, Jing Q, Poeppelmeier KR, Rondinelli JM. $Cs_3Zn_6B_9O_{21}$: A chemically benign member of the KBBF family exhibiting the largest second harmonic generation response. *J Am Chem Soc*. 2014;136(4):1264–1267.
38. Mutailipu M, Xie ZQ, Su X, Zhang M, Wang Y, Yang ZH, Janjua MRSA, Pan SL. Chemical cosubstitution-oriented design of rare-earth borates as potential ultraviolet nonlinear optical materials. *J Am Chem Soc*. 2017;139(50):18397–18405.
39. Wu HP, Yu HW, Zhang WG, Cantwell J, Poeppelmeier KR, Pan SL, Halasyamani PS. Top-seeded solution crystal growth and linear and nonlinear optical properties of $Ba_4B_{11}O_{20}F$. *Cryst Growth Des*. 2017;17(3):1404–1410.
40. Yu HW, Wu HP, Pan SL, Yang ZH, Su X, Zhang FF. A novel deep UV nonlinear optical crystal $Ba_3B_6O_{11}F_2$, with a new fundamental building block, B_6O_{14} group. *J Mater Chem*. 2012;22(19):9665–9670.
41. Zhao SG, Gong PF, Bai L, Xu X, Zhang SQ, Sun ZH, Lin ZS, Hong MC, Chen CT, Luo JH. Beryllium-free $Li_4Sr(BO_3)_2$ for deep-ultraviolet nonlinear optical applications. *Nat Commun*. 2014;5:4019.
42. Zhao SG, Yang XY, Yang Y, Kuang XJ, Lu FQ, Shan P, Sun ZH, Lin ZS, Hong MC, Luo JH. Non-centrosymmetric $RbNaMgP_2O_7$ with unprecedented Thermo-induced enhancement of second harmonic generation. *J Am Chem Soc*. 2018;140(5):1592–1595.
43. Mutailipu M, Zhang M, Wu HP, Yang ZH, Shen YH, Sun JL, Pan SL. $Ba_3Mg_3(BO_3)_3F_3$ polymorphs with reversible phase transition and high performances as ultraviolet nonlinear optical materials. *Nat Commun*. 2018;9:3089.
44. Mori Y, Kuroda I, Nakajima S, Sasaki T, Nakai S. New nonlinear optical crystal: Cesium lithium borate. *Appl Phys Lett*. 1995;67(13):Article 1818.
45. Ye N, Zeng WR, Jiang J, Wu BC, Chen CT. New nonlinear optical crystal $K_2Al_2B_2O_7$. *J Opt Soc Am B*. 2000;17:764–768.
46. Zhao SG, Gong PF, Luo SY, Bai L, Lin ZS, Ji CM, Chen TL, Hong MC, Luo JH. Deep-ultraviolet transparent phosphates $RbBa_2(PO_3)_5$ and $Rb_2Ba_3(P_2O_7)_2$ show nonlinear optical activity from condensation of $[PO_4]^{3-}$ Units. *J Am Chem Soc*. 2014;136(24):8560–8563.
47. Wang XF, Wang Y, Zhang BB, Zhang FF, Yang ZH, Pan SL. CsB_4O_6F: A congruent-melting deep-ultraviolet nonlinear optical material by combining superior functional units. *Angew Chem Int Ed*. 2017;56(45):14119–14123.
48. Peng G, Ye N, Lin ZS, Kang L, Pan SL, Zhang M, Lin CS, Long XF, Luo M, Chen Y, et al. $NH_4Be_2BO_3F_2$ and γ-Be_2BO_3F: Overcoming the layering habit in $KBe_2BO_3F_2$ for the next-generation deep-ultraviolet nonlinear optical materials. *Angew Chem Int Ed*. 2018;57(29):8968–8972.
49. Oseledchik YS, Prosvirnin AL, Pisarevskiy AI, Starshenko VV, Osadchuk VV, Belokrys SP, Svitanko NV, Korol AS, Krikunov SA, Selevich AF. New nonlinear optical crystals: Strontium and lead tetraborates. *Opt Mater*. 1995;4(6):669–674.
50. Wang Y, Zhang BB, Yang ZH, Pan SL. Cation-tuned synthesis of fluorooxoborates: Towards optimal deep-ultraviolet nonlinear optical materials. *Angew Chem Int Ed*. 2018;57(8):2150–2154.
51. Xia MJ, Jiang XX, Lin ZS, Li RK. "All-three-in-one": A new bismuth–tellurium–borate Bi_3TeBO_9 exhibiting strong second harmonic generation response. *J Am Chem Soc*. 2016;138(43):14190–14193.
52. Zou GH, Huang L, Ye N, Lin CS, Cheng WD, Huang H. $CsPbCO_3F$: A strong second-harmonic generation material derived from enhancement via p–π interaction. *J Am Chem Soc*. 2013;135(49):18560–18566.
53. Cong RH, Wang Y, Kang L, Zhou ZY, Lin ZS, Yang T. An outstanding second-harmonic generation material BiB_2O_4F: Exploiting the electron-withdrawing ability of fluorine. *Inorg Chem Front*. 2015;2(2):170–176.
54. Luo M, Liang F, Song YX, Zhao D, Ye N, Lin ZS. Rational design of the first lead/tin fluorooxoborates $MB_2O_3F_2$ (M = Pb, Sn), containing flexible two-dimensional $[B_6O_{12}F_6]_\infty$ single layers with widely divergent second harmonic generation effects. *J Am Chem Soc*. 2018;140(22):6814–6817.
55. Chen CT, Wu BC, Jiang AD, You GM. A new-type ultraviolet SHG crystal——β-BaB_2O_4. *Sci Sin B*. 1985;28(3):235–243.
56. Wu HP, Pan SL, Poeppelmeier KR, Li HY, Jia DZ, Chen ZH, Fan XY, Yang Y, Rondinelli JM, Luo HS. $K_3B_6O_{10}Cl$: A new structure analogous to perovskite with a large second harmonic generation response and deep UV absorption edge. *J Am Chem Soc*. 2011;133(20):7786–7790.
57. Wu Y, Fu P, Wang J, Xu Z, Zhang L, Kong Y, Chen C. Characterization of CsB_3O_5 crystal for ultraviolet generation. *Opt Lett*. 1997;22(24):1840–1842.
58. Lin SJ, Sun ZY, Wu BC, Chen CT. The nonlinear optical characteristics of a LiB_3O_5 crystal. *J Appl Phys*. 1990;67(2):634.
59. Shi GQ, Wang Y, Zhang FF, Zhang BB, Yang ZH, Hou XL, Pan SL, Poeppelmeier KR. Finding the next deep-ultraviolet nonlinear optical material: $NH_4B_4O_6F$. *J Am Chem Soc*. 2017;139(31):10645–10648.
60. Chen ZH, Pan SL, Yang ZH, Dong XY, Su X, Yang Y. $Pb_2B_5O_9Cl$: A chloride borate with second harmonic generation effect. *J Mater Sci*. 2012;48:2590–2596.
61. Han SJ, Mutailipu M, Tudi A, Yang ZH, Pan SL. $PbB_5O_7F_3$: A high-performing short-wavelength nonlinear optical material. *Chem Mater*. 2020;32(5):2172–2179.
62. Reckeweg O, Schulz A, DiSalvo FJ. Orthoborate halides with the formula $(M^{+II})_5(BO_3)_3X$: Syntheses, crystal structures and Raman spectra of $Eu_5(BO_3)_3Cl$ and $Ba_5(BO_3)_3X$ (X = cl, Br). *Z Naturforsch, B Chem Sci*. 2011;66:359–365.
63. Chen ZH, Pan SL, Zhao WW, Yang Y, Wu HP, Zhang FF. Study on synthesis, crystal growth and properties of nonlinear optical crystal $Ba_2B_5O_9Cl$. *J Synth Cryst*. 2011;40:1394.
64. Huang CM, Zhang FF, Li H, Yang ZH, Yu HH, Pan SL. $BaB_2O_3F_2$: A barium Fluorooxoborate with a unique $^2_\infty[B_2O_3F]^-$ layer and short cutoff edge. *Chem Eur J*. 2019;25(27):6693–6697.
65. Henkelman G, Arnaldsson A, Jónsson H. A fast and robust algorithm for Bader decomposition of charge density. *Comput Mater Sci*. 2006;36(3):354–360.
66. Tang W, Sanville E, Henkelman G. A grid-based Bader analysis algorithm without lattice bias. *J Phys Condens Matter*. 2009;21:Article 084204.
67. Chan MKY, Ceder G. Efficient band gap prediction for solids. *Phys Rev Lett*. 2010;105(19):Article 196403.

68. Krukau AV, Vydrov OA, Izmaylov AF, Scuseria GE. Influence of the exchange screening parameter on the performance of screened hybrid functionals. *J Chem Phys*. 2006;125(125):Article 224106.
69. Walsh A, Payne DJ, Egdell RG, Watson GW. Stereochemistry of post-transition metal oxides: Revision of the classical lone pair model. *Chem Soc Rev*. 2011;40(9):4455–4463.
70. Li DN, Jing Q, Lei C, Pan SL, Zhang BB, Yang ZH. Theoretical perspective of the lone pair activity influence on band gap and SHG response of Lead borates. *RSC Adv*. 2015;5(97):79882–79887.
71. Lin J, Lee M-H, Liu Z-P, Chen CT, Pickard CJ. Mechanism for linear and nonlinear optical effects in β – BaB_2O_4 crystals. *Phys Rev B*. 1999;60(19):13380–13389.
72. Kurtz SK, Perry TT. A powder technique for the evaluation of nonlinear optical materials. *J Appl Phys*. 1968;39(8):3798.
73. Clark SJ, Segall MD, Pickard CJ, Hasnip PJ, Probert MIJ, Refson K, Payne MC. First principles methods using CASTEP. *Z Kristallogr*. 2005;220:567–570.
74. Perdew JP, Burke K, Ernzerhof M. Generalized gradient approximation made simple. *Phys Rev Lett*. 1996;77(18):3865–3868.
75. Rappe AM, Rabe KM, Kaxiras E, Joannopoulos JD. Optimized pseudopotentials. *Phys Rev B*. 1990;41(2):1227–1230.
76. Lin ZS, Jiang XX, Kang L, Gong PF, Luo SY, Lee M-H. First-principles materials applications and design of nonlinear optical crystals. *J Phys D Appl Phys*. 2014;47:Article 253001.